

Measurements, simulations, and models of the point-spread function of electron-beam lithography

Nikolaj B. Hougs^{1*}, Kristian S. Knudsen¹, Marcus Albrechtsen¹, Taichi Suhara²,
Christian A. Rosiek¹, Søren Stobbe^{1,3,4}

¹DTU Electro, Department of Electrical and Photonics Engineering, Technical University of Denmark, Ørsteds Plads 343, Kgs. Lyngby, DK-2800, Denmark.

²ELIONIX INC., 3-7-6 Motoyokoyama-cho Hachioji, Tokyo, 192-0063 Japan.

³NanoPhoton — Center for Nanophotonics, Technical University of Denmark, Ørsteds Plads 343, Kgs. Lyngby, DK-2800, Denmark.

⁴Beamfox Technologies ApS, Njalsgade 76, 4., Copenhagen S, DK-2300, Denmark.

*Corresponding author(s). E-mail(s): nibaho@dtu.dk;

Abstract

When a sample is exposed using electron-beam lithography, the electrons scatter deep and far in the substrate, resulting in unwanted deposition of dose at both the nano- and the microscale. This proximity effect can be mitigated by proximity effect correction provided that accurate and validated models of the point-spread function of the electron scattering are available. Most works so far considered a double-Gaussian model of the electron point-spread function, which is very inaccurate for modern electron-beam writers with high acceleration voltages. We present measurements of the process point-spread function for chemically semi-amplified resist on silicon and indium phosphide substrates using a 150 kV electron-beam lithography system. We find that the double-Gaussian model deviates from experiments by up to four orders of magnitude. We propose instead a model comprising the sum of a power-law and a Gaussian, which is in excellent agreement with simulations of the electron scattering obtained by a Monte Carlo method. We apply the power-law plus Gaussian model to quantify the electron scattering and proximity effect correction parameters across material stacks, processing, and voltages from 5 kV to 150 kV. We find that the power-law term remains remarkably constant, whereas the long-range dose contributions and the clearing dose are significantly affected by the substrate and the acceleration voltage.

Keywords: Electron-beam lithography, electron point-spread function, Monte Carlo simulation, nanotechnology, nanofabrication

Introduction

Electron-beam lithography (EBL)^{1,2} is central to modern nanofabrication as it is the workhorse for both direct-write prototyping in research and for the production of master masks for deep or extreme ultraviolet lithography^{1,3} and nanoimprint lithography^{1,4,5}. The serial exposure of EBL is slower in comparison, although faster writing speeds are obtained in shaped-beam systems⁶, multi-beam systems⁷, and low-voltage systems⁸. For high-resolution lithography, the method of choice is single-shot Gaussian-beam EBL using high acceleration voltages^{9–11}.

The purpose of EBL is to deposit energy and induce chemical changes in an electron-sensitive resist¹², which, after development and subsequent processing such as etching and deposition, results in a mapping of the input mask onto the physical device. However, this mapping is distorted by three effects: Shot-filling errors, the proximity effect, and process effects, as illustrated in Fig. 1.

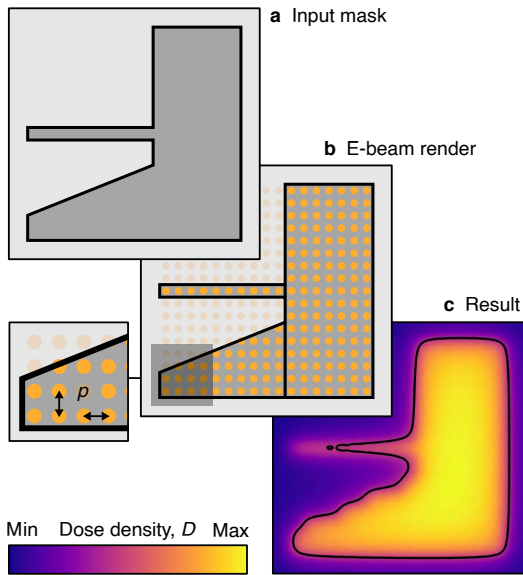


Figure 1 Impact of shot filling and proximity effects on electron-beam lithography. (a) An input mask containing the intended pattern is rendered as (b) polygonal exposure primitives. In Gaussian-beam lithography, the polygons are exposed as arrays of shots on a discrete grid (orange dots). (c) The fabricated pattern deviates from the input mask due to three effects: Shot-filling errors, proximity effects, and process effects due to development as well as any subsequent etching and deposition.

Shot-filling errors arise when the input mask is fractured into simple polygons, which, in Gaussian-beam EBL, are further fractured into arrays of shots. In principle, shot-filling errors can be eliminated by using sufficiently small shot pitches, but in practice, limitations in most EBL systems as well as considerations about writing time prevent using shot pitches below a nanometer. Although some EBL systems offer features such as shaped beams or additional primitives such as circles, these features cannot fully circumvent shot-filling errors. The only robust solution across all types of EBL systems is to ensure that the input mask consists only of rectangles, whose edges are aligned to the coordinate system of the EBL writer and whose side lengths are integer values of the shot pitch¹³.

The proximity effect is much harder to correct for, as it cannot be removed at the design level, and proximity effect correction is a hard inverse mathematical problem. The proximity effect is governed by the spatial distribution of deposited energy from a point exposure, *i.e.*, the electron point-spread function (PSF)^{14–17}. The issue of the proximity effect and the development of approaches to proximity effect correction (PEC) have therefore been a central element of EBL research since its conception^{18–27}.

The PSF depends sensitively on the material stack and exposure parameters such as the acceleration voltage. It can be expanded to a process-specific PSF (PPSF) to include additional effects, such as beam size, resist-development chemistry, time, and temperature as well as the subsequent lithographic steps, *e.g.*, etching²⁸ or deposition^{29,30}. It is important to stress that even the simplest practical example of EBL includes at least two effects that go beyond the PSF: The finite waist of the electron beam and the development. In practice, this means only the PPSF can be measured.

In an EBL point exposure, an electron beam impinges on a resist layer on a substrate, see Fig. 2(a). The physics underlying the electron scattering in the resist and the substrate is complex, involving secondary electrons and volume plasmons^{31–34}, and the proximity effect is therefore commonly modeled using a stochastic Monte Carlo approach^{35–38} such as the simulations shown in Fig. 2(b) and (c). The resist is

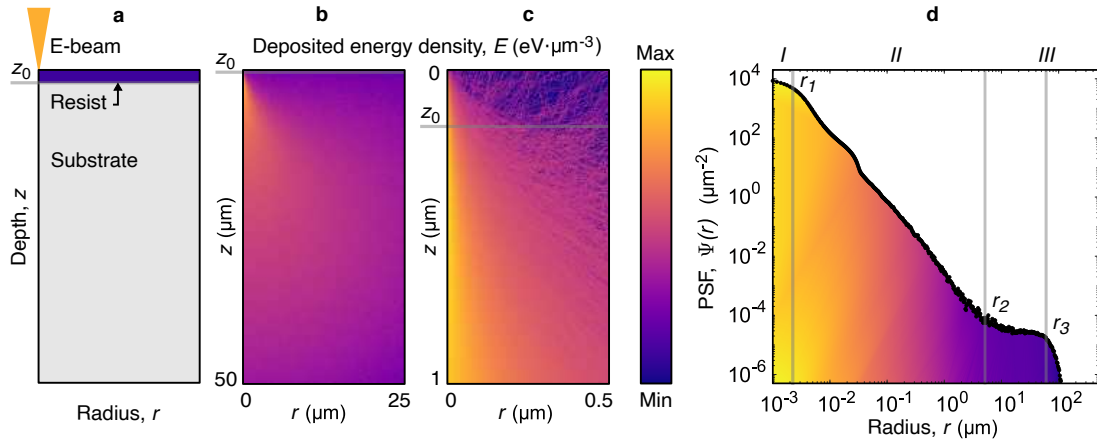


Figure 2 The electron point-spread function (PSF) in electron-beam lithography. (a) Illustration in cylindrical coordinates of electrons impinging on a stack consisting of resist on a substrate. (b)-(c) Monte Carlo simulation of electron scattering and the corresponding deposited dose distribution from one million 150 kV electrons impinging on a resist-silicon stack. (d) When considering only the energy deposition in the resist, the PSF is only a function of the radius, and three distinct regions, *I-III*, can be identified as discussed in the main text.

normally much thinner (a few hundred nanometers) than the scattering length (tens of microns), so it is often a good approximation to consider only the PSF as being invariant of depth in the resist, in which case the PSF becomes a function of only the radius, r , as shown in Fig. 2(d). We identify three distinct regions as indicated in the figure: *I*, for very short ranges, the PSF is relatively flat; *II*, for intermediate ranges, the PSF approximately follows a power-law³⁹; *III*, for long ranges, the PSF falls off rapidly.

Ignoring region *II* and separating dose contributions into incident and backscattering⁴⁰, may suggest a double-Gaussian (2G) model which is common in the literature^{11,14,15,18-25}, but this model is an oversimplification. Nevertheless, since only ad-hoc methods exist today for short- and intermediate-range PEC, a common approach to PEC is to use automatic dose modulation for long-range effects^{41,42} combined with manual shape correction for short-range effects^{13,43-45}. Although this relies on tedious trial and error for the short-range PEC, it can eventually be an effective strategy. However, this is not an optimal solution, and previous works have improved on the 2G model by adding exponential¹⁵ or Gaussian terms⁴⁶⁻⁴⁸. For numerical calculations, a multi-Gaussian fit may be useful, but such fits inevitably include many parameters that impede assessments of resolution limits and quantitative comparisons between different processes across different hardware and material platforms.

Here we present accurate measurements of the PPSF for chemically semi-amplified resist (CSAR)⁴⁹ on both silicon and indium phosphide (InP) substrates at 150 kV using single-shot exposures. We find excellent agreement with Monte Carlo simulations of the PSF except for distances below 10 nm, which indicates that the PSF and PPSF are identical except at very short distances. We propose an empirical power-law plus Gaussian (PLG) model of the PSF, and we demonstrate a greatly improved agreement with experiment over 10 orders-of-magnitude of deposited dose, corresponding to 5 orders-of-magnitude of distances from 1 nm-100 μm for both silicon and InP substrates.

Results and discussion

Measuring the point-spread function

Before discussing our experiment, we briefly outline the theory of EBL and the theoretical foundation for extracting the PSF, building in part on Refs. 14,15. The purpose of EBL is to map a mask, $M(x, y)$, onto a physical device with the greatest possible fidelity. In Gaussian-beam EBL, the mask is rendered as a shot map

$$S(x, y, p) = p^2 \sum_{i,j} \delta(x - ip) \delta(y - jp) M(x, y), \quad (1)$$

where $p = p_x = p_y$ is the shot pitch. It is desirable to choose p much smaller than the smallest critical dimension of the mask to minimize shot-filling errors. Each shot is broadened according to the PSF, $\Psi(r)$, which is related to the density of energy deposited in the resist, $E(r)$, as

$$\Psi(r) = \frac{E(r)}{2\pi \int E(r) r dr}. \quad (2)$$

The PSF is a probability density with normalization $2\pi \int \Psi(r) r dr = 1$. We refer to the Supporting Information for additional details on extracting the PSF from simulations of $E(r)$. In practice, the energy is often replaced by an effective deposited charge dose density

$$D(r) = k^{-1} E(r), \quad (3)$$

with k a charge-to-energy conversion factor that is constant for a given process and exposure condition. With these definitions, the deposited dose distribution is given by

$$D(x, y) = D_{\text{in}} \Psi(r) * S(x, y, p), \quad (4)$$

where $*$ denotes the convolution, and D_{in} is the impinging charge dose density, which is directly related to the impinging shot charge, $q_{\text{in}} = p^2 D_{\text{in}}$. Thus, if no PEC is applied, the convolution of $S(x, y, p)$ with $\Psi(r)$ distorts $D(x, y)$. The purpose of PEC is to transform $S(x, y, p)$ and/or apply a spatial variation to D_{in} , such that $D(x, y)$ becomes as close to the input mask as possible. After development, the resist is fully cleared where

$$D(x, y) \geq D_0, \quad (5)$$

with D_0 the clearing dose, which is the minimum dose required to clear the center of a polygon whose size is much larger than any length scales in the PSF. An advantage of this definition is that the clearing dose is pattern-independent, *i.e.*, in the center of a sufficiently large polygon, $D(x, y)$ becomes equal to D_{in} . Note that D_0 depends on the material stack, acceleration voltage, and development conditions.

The exposed pattern can only be imaged after development, which implies that an experiment probes the PPSF rather than the PSF. It is useful to consider an isolated shot, where the shot

map reduces to $S(x, y, p) = p^2 \delta(x, y)$ and Eq. (4) reduces to

$$D(r, p) = p^2 D_{\text{in}} \Psi(r) = q_{\text{in}} \Psi(r), \quad (6)$$

Combined with Eq. (5), this ensures that the resist is fully developed out to a radius r_0 , such that the PPSF can be obtained from a sequence of single-shot exposures with different q_{in} using

$$\Psi(r_0) = \frac{D_0}{q_{\text{in}}}. \quad (7)$$

Measuring the clearing dose

Turning to the experiment, we first expose a set of large squares with different uniform doses as illustrated in Fig. 3(a). Figure 3(b-c) shows bright- and dark-field optical-microscopy (OM) images of the exposed and developed pattern with insets for $D_{\text{in}} = 225 \mu\text{C}/\text{cm}^2$. The median of the normalized pixel intensity I_p is computed from the central cutouts of Fig. 3(d-e). This is used to determine the clearing dose, $D_0 = 225 \pm 5 \mu\text{C}/\text{cm}^2$, as the dose with no remaining resist, *i.e.*, we observe no change in pixel intensity when increasing the dose further, based on an empirical condition for the gradient, $\nabla I_p \leq 0.05$, being fulfilled for $D_{\text{in}} \geq D_0$, see Fig. 3(f).

Measurement of the process point-spread function from point exposures

Having determined D_0 , we now consider the measurement of the PPSF according to Eq. (7). We therefore expose sequences of points as illustrated schematically in Fig. 4(a), which shows two point exposures of charge $q_{\text{in},1} < q_{\text{in},2}$, separated by a distance d large enough to consider each exposure isolated, such that development removes resist out to radii $r_{0,1} < r_{0,2}$. We then use scanning electron microscopy (SEM) and OM images of the developed holes to measure the radii r_0 as shown in Fig. 4(b-d). This method benefits from its conceptual simplicity but the resolution of SEM is insufficient to accurately measure holes resulting from impinging shot charges below $q_{\text{in}} = 6 \text{ fC}$. For high doses, a central pillar becomes cross-linked as can be seen in Fig. 4(d) and may even topple over, which is apparent from a careful inspection of Fig. 4(c). To extract the radii of the developed

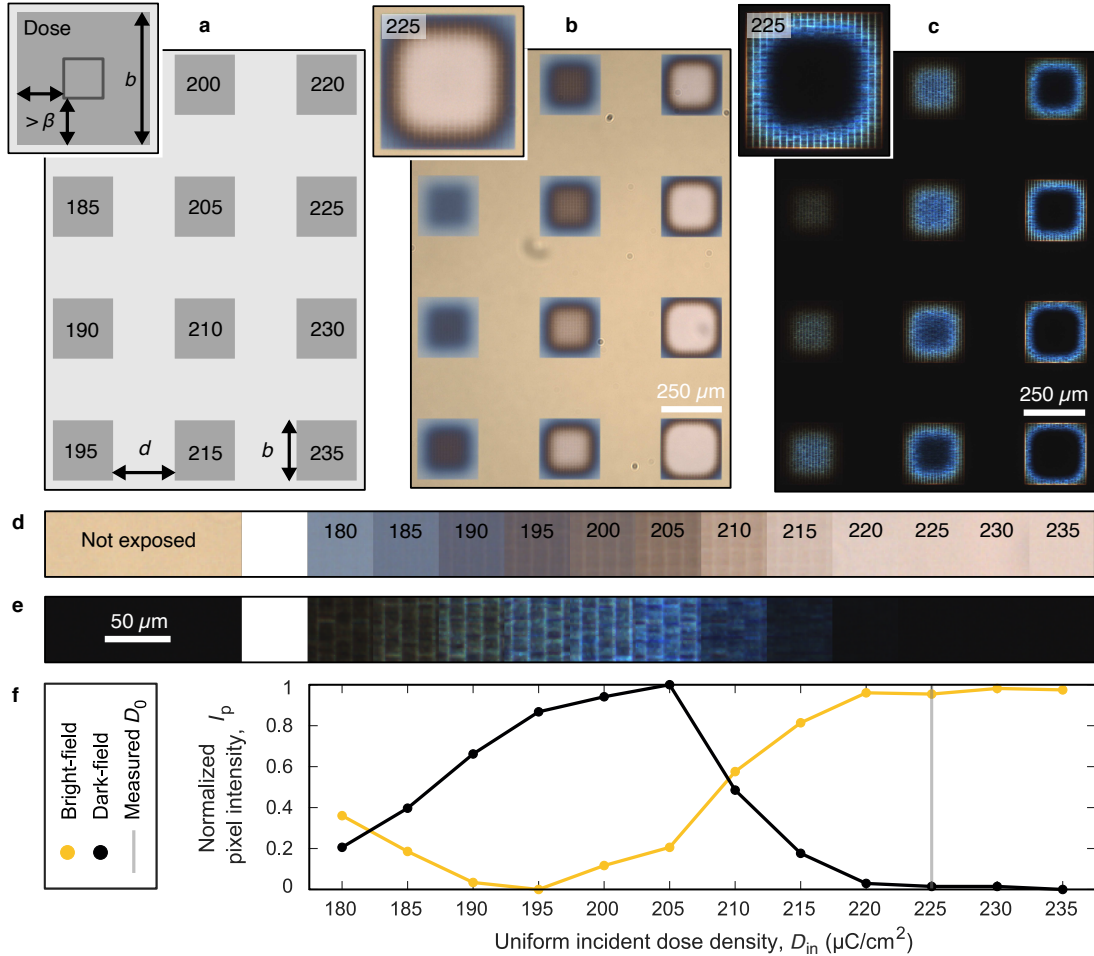


Figure 3 Measurement of the clearing dose, D_0 , for 150 kV exposures on a stack comprising 180 nm CSAR on silicon. (a) A mask containing squares with uniform incident doses indicated as the numbers in units of $\mu\text{C}/\text{cm}^2$. Both the size of the squares, b , and the distance between them, d , are chosen to be much larger than β , where β is the radius characterizing the long-range part of the PSF. These conditions ensure that in the center of the squares, the deposited doses are equal to the uniform incident doses. (b) Bright-field optical micrograph of the device after exposure and development, where the remaining resist thickness determines the color. (c) Dark-field optical micrograph of the same region as in (b). The overlapping subfields from the exposure are visible as a mesh for doses close to the clearing dose. (d)-(e), Cutouts of the central $50 \times 50 \mu\text{m}^2$ regions of the exposed squares. (f) Extraction of the clearing dose as the minimum dose where the intensities from (d) and (e) are independent of dose, which is consistent across both the bright- and dark-field data sets.

holes, we use image analysis as explained in the Supporting Information.

The measured PPSF is shown in Fig. 4(e). In order to reduce the writing time for the longer exposures, two different currents, $I = 0.1 \text{ nA}$ and $I = 10 \text{ nA}$, are used for the experiment. We observe that the measured PPSF at $I = 10 \text{ nA}$ is higher than at $I = 0.1 \text{ nA}$ in the range of 5 nm-50 nm. We note that this cannot be explained solely by differences in beam waist resulting from the different apertures used for the two currents, because such broadening should be included as

convolutions that would preserve the normalization. Instead, we observe a systematically higher PPSF for $I = 10 \text{ nA}$ such that its integral is not preserved. This could indicate that the development rate depends weakly on the exposure current, which is not included in the theoretical framework outlined above, and could be attributed to radiation damage or similar effects. This shows that, at least for CSAR resist, one must be careful when switching between currents. In practice, lower currents are used for small features because of intrinsically smaller spot sizes and

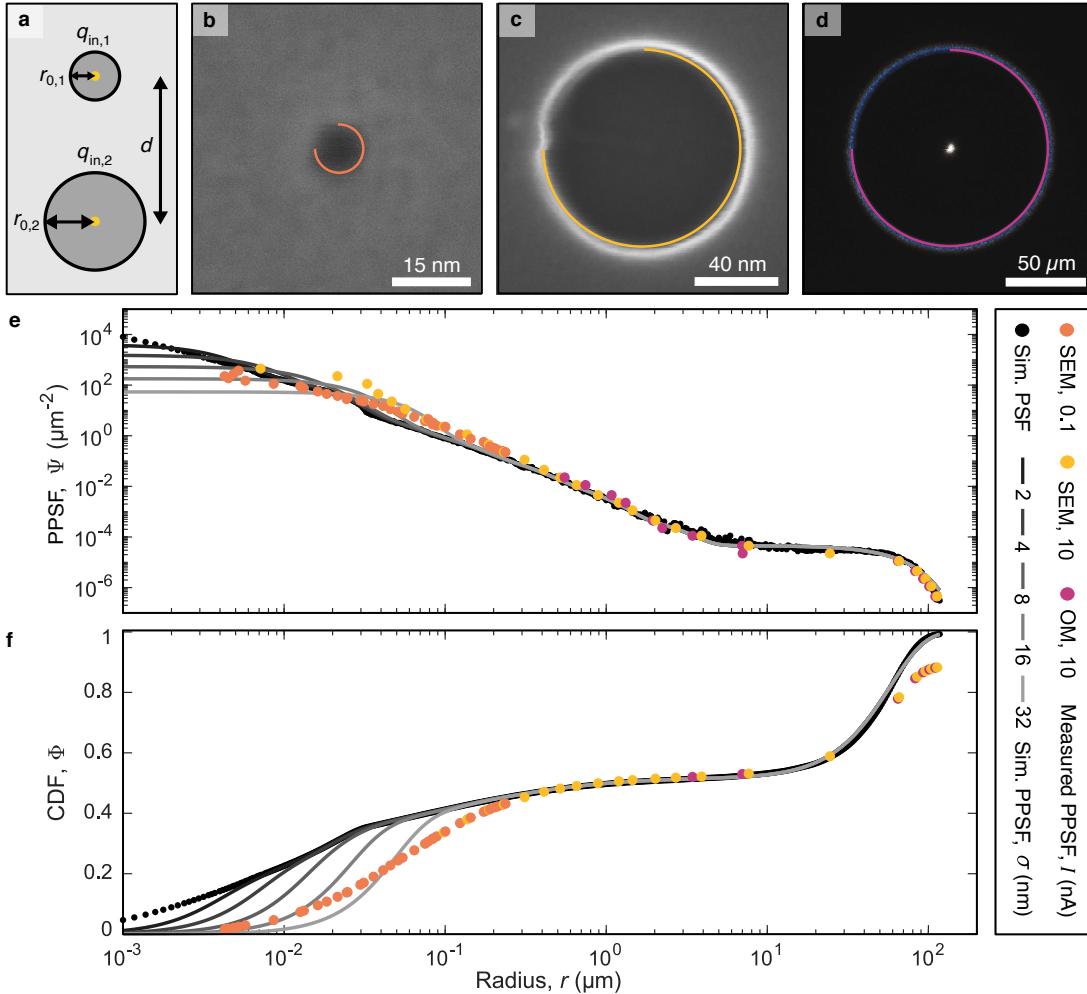


Figure 4 Measurement of the process point-spread function (PPSF). We consider the same parameters as in Fig. 3, *i.e.*, 150 kV exposures on a stack comprising 180 nm CSAR on silicon. (a) Illustration of two isolated points exposed with shot charges, $q_{in,1} < q_{in,2}$, such that the resist is fully developed out to radii of $r_{0,1} < r_{0,2}$. To avoid the two areas affecting each other through the proximity effect, they are separated by a distance $d \gg r_{0,2}$. (b)-(c) Scanning electron microscopy (SEM) and (d) optical microscopy (OM) images of the developed patterns. The exposed holes are fitted to obtain the outline (colored 3/4 circles) and radii. (e) The deposited charge as a function of the measured radius, *i.e.*, the PPSF obtained by varying the deposited charge (colored dots). Two different currents, I , are used to reduce the writing time for very large radii. Except for a few points at shorter radii, the analysis by OM and SEM give very similar results, which in turn agree very well with the the PSF extracted from a Monte Carlo simulation (black dots). The deviations for radii below 50 nm could originate from process effects. By convolving the PSF with Gaussians of different standard deviations, σ , simulated PPSFs that include the beam distribution are obtained (solid lines). (f) The cumulative density functions (CDFs) of the PPSFs emphasize the deviations, as well as the varying contributions to the deposited dose across the PPSFs.

minimum-dwell-time limits, so we consider the PPSF at $I = 0.1$ nA more representative at short ranges. Additional details on the data analysis is included in the Supporting Information.

Figure 4(e) shows also the PSF obtained from Monte Carlo simulations. We observe excellent agreement except at very short radii, given that the data set extends over so many orders of magnitude. For the same reason, the apparent agreement

may be misleading, as a few experimental points actually deviate from the simulation by more than an order of magnitude. In order to investigate whether the finite beam waist is responsible for the deviations between the simulated PSF and the measured PPSF at small radii, we convolve the PSF with Gaussians of different widths as shown in Fig. 4(e). While this provides a slightly better

agreement with the PPSF, the lack of data points below 4 nm make this comparison inconclusive.

The several orders of magnitude covered by the PPSF hide its nuances, some of which become clearer by also considering its cumulative density function (CDF),

$$\Phi(r) = 2\pi \int_0^r \Psi(\tilde{r}) \tilde{r} d\tilde{r}, \quad (8)$$

which represents the fraction of the total dose deposited out to a given range. Importantly, simulations or models of the PPSF also need to accurately represent the CDF, which is complicated by the fact that seemingly minor changes in the PPSF, due to its scale, can significantly impact the CDF. The CDF estimated by trapezoidal numerical integration of the data in Fig. 4(e) is shown in Fig. 4(f). Notably, the integral of the measured PPSF, *i.e.*, the maximum value of the CDF, is $\max(\Phi) = 0.88$. Shot noise adds uncertainty to q_{in} , but this noise averages out to less than 1% for all doses measured in our experiment. Nevertheless, multiple other factors could explain the deviation from the ideal value of unity: One is the above-mentioned current-dependency. A second is numerical errors associated with integrating a function over so many orders of magnitude. A third is errors in the measurement of r_0 , which may be biased by, *e.g.*, sidewall inclinations, line-edge roughness, and SEM artefacts. This is particularly pronounced for very small and very large radii. Finally, hydrodynamic effects may impact the development for the smallest radii as diffusion in and out of the tiny holes is slowed down, or impact the measurement of D_0 due to forces at the resist-substrate interface. In the rest of this paper, we normalize the measured CDFs as $\Phi/\max(\Phi)$ to evenly distribute errors from any of these effects.

Models of the process point-spread function at high acceleration voltages

For a quantitative description of the PPSF, the model most commonly used is the 2G model,

$$\Psi_{2G}(r) = \frac{1}{\pi(1+\eta)} \left[\frac{1}{\alpha^2} e^{-\frac{r^2}{\alpha^2}} + \frac{\eta}{\beta^2} e^{-\frac{r^2}{\beta^2}} \right], \quad (9)$$

where the standard deviations $\alpha/\sqrt{2}$ and $\beta/\sqrt{2}$ respectively represent the dose deposited by

the forward-scattered electrons and the electrons back-scattered from the substrate into the resist, with η describing their relative contribution. The advantages of the 2G model include simplicity and numerical speed. It is also possible to extract reasonable estimates of η and β for PEC by fitting the 2G model to the long-range PPSF or CDF while setting $\alpha = 0$. Figure 5 shows the same data as in Fig. 4 compared to different models of the PPSF. The 2G model agrees well with the PPSF for large radii but fails at shorter radii, in particular in the intermediate range where it deviates by up to four orders of magnitude.

On this background, we propose replacing the forward Gaussian with a power law, resulting in a power-law plus Gaussian (PLG),

$$\Psi_{\text{PLG}}(r) = \frac{1}{\pi(1+\eta)} \left[\frac{\nu^{-2}}{\left(\frac{r}{\gamma}\right)^\sigma + e^{\frac{r^2}{(\beta/4)^2}}} + \frac{\eta}{\beta^2} e^{-\frac{r^2}{\beta^2}} \right], \quad (10)$$

where $\beta/\sqrt{2}$ remains the standard deviation of the long-range scattering, η is now the ratio of short- and intermediate- to long-range scattering (both can be inserted directly into a 2G model), γ is the radius at half maximum of the forward distribution and marks the beginning of the power-law scaling, σ is the slope of the power law and ν is the normalization constant of the power-law term. The denominator of the power-law term includes an empirical Gaussian cut-off term to ensure that the long-range Gaussian dominates at $r \gg \beta$ and to avoid a singularity at $r = 0$ nm.

The parameters of the PLG model define the regions *I-III*: The short-range limit, $r_1 = \gamma$; the radius at which the two model terms are equal, r_2 , *i.e.*, the intermediate- to long-range boundary; and the characteristic radius of the long-range distribution, $r_3 = \beta$. These are shown together with a fit to the PLG model in Fig. 5. The PLG model shows excellent agreement with the measured PPSF, although minor systematic deviations remain in the short-to-intermediate range and beyond β . For comparison, the 2G model in Fig. 5 is chosen to have the same values of η and β as the PLG model fit, as well as a value for α that replicates the short-range behavior. We refer to the Supporting Information for further details on the fitting procedure.

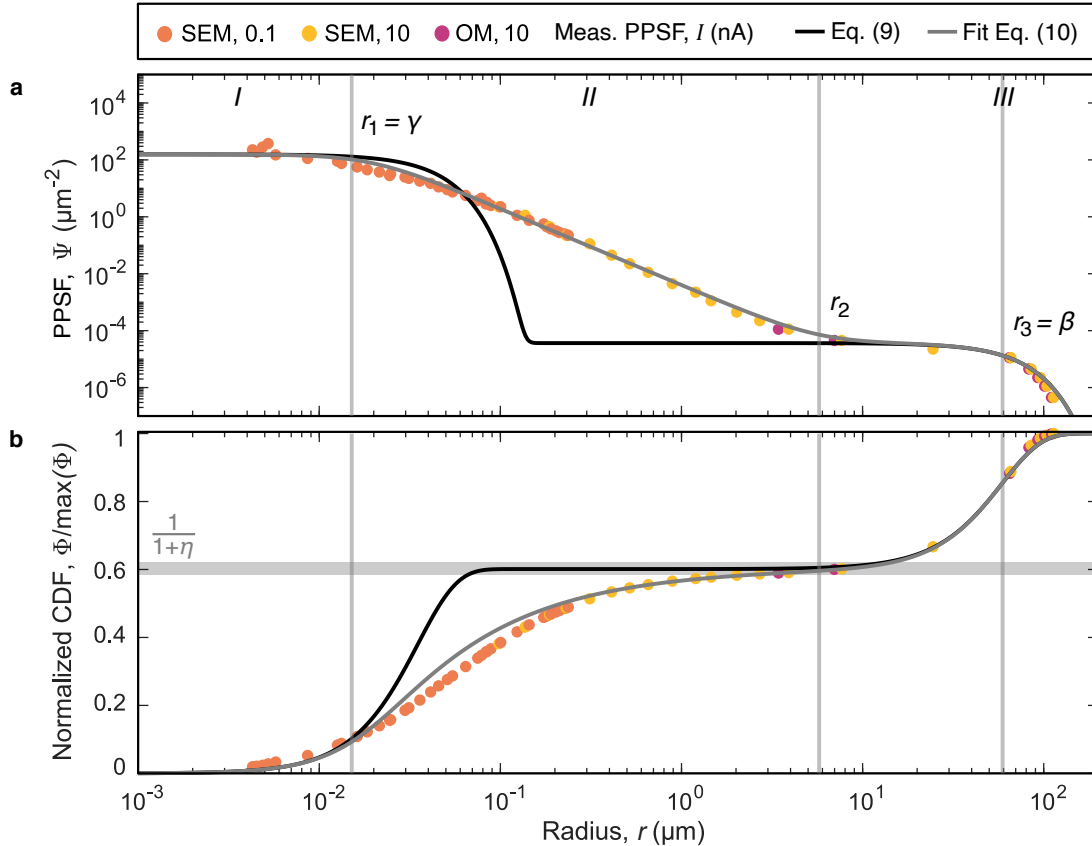


Figure 5 Comparison of theoretical models of the process point-spread function (PPSF). We consider the same parameters as in Fig. 3, *i.e.*, 150 kV exposures on a stack comprising 180 nm CSAR on silicon. (a) The measured PPSF (orange, yellow, and purple dots) is fitted with a power-law plus Gaussian (PLG) model (grey line) with excellent agreement. The commonly employed double-Gaussian (2G) model (black line) deviates from measurements by up to four orders of magnitude. The three regions *I-III* introduced in Fig. 2(d) are well-defined in the PLG model: The radius at half maximum, $\gamma = r_1$, the radius at which the two model terms are equal, r_2 , and the characteristic radius of the long-range Gaussian term, $\beta = r_3$. (b) The corresponding cumulative density functions (CDFs) of the PLG and 2G models coincide for $r > r_2$.

Importantly, the PLG model also accurately captures η in the CDF. Here the maximum value of the power-law term, $\Phi = (1 + \eta)^{-1}$, clearly distinguishes the short- to intermediate-range dose contribution from that of the long range. This means that we can consider regions *I-II* and *III* separately for PEC: When patterns are fractured into polygons of sizes larger than r_2 , the proximity effect from one polygon to another is solely governed by the long-range Gaussian, and the proximity effect of the polygons onto themselves, *i.e.*, the so-called self-dose, is solely governed by the short-to-intermediate ranges and reduces to $(1 + \eta)^{-1}$. This is a too coarse fracturing for high-resolution lithography, but it can be applied away from polygon edges. Conversely, the long-range Gaussian does not contribute to the self-dose for polygons

smaller than r_2 . For practical applications, the PLG model can give an accurate estimate of the η parameter, which is essential to many PEC algorithms, but its main purpose is as a simple model to allow for detailed comparisons between different material stacks, acceleration voltages, and process parameters.

Measurements of the 150 kV process point-spread functions for longer development, aluminum decharging layer and indium phosphide substrate

In order to compare the effects of different material systems and process parameters, we measure the PPSF in three additional experiments, each one modifying one parameter:

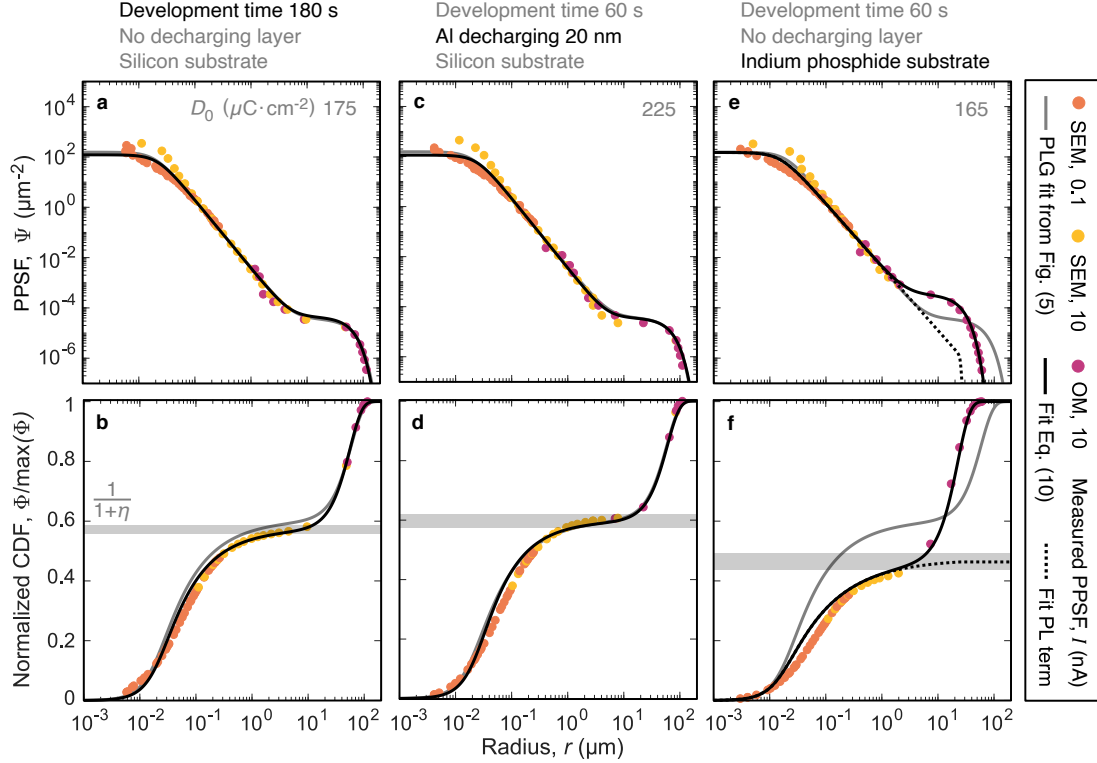


Figure 6 Process point-spread functions (PPSFs) and the corresponding cumulative density functions (CDFs) for 150 kV exposures on 180 nm CSAR with varying material stacks and processing parameters. Measured PPSFs (colored dots) are well reproduced by fits (black lines) with a power-law plus Gaussian (PLG). The clearing dose, D_0 extracted from a corresponding dose test (not shown) is indicated for each experiment. The PLG fit to the results presented in Figs. 3-5 is shown for comparison (grey lines). (a)-(b) An increased development time lowers the clearing dose, but affects the PPSF minimally. (c)-(d) A 20 nm aluminum decharging layer on top of the resist during electron-beam exposure results in a negligible change. (e)-(f) An indium phosphide substrate instead of silicon significantly decreases the clearing dose and changes the PPSF: The long-range contribution falls off at shorter radii, but contributes relatively more to the deposited dose as seen from the CDF, which is attributed to increased electron scattering in the denser substrate.

1. Tripling the development time, which should reduce the clearing dose, D_0 , but retain the same deposited dose distribution, $D(r)$, and thus the same PSF.
2. Adding a 20 nm an aluminum layer on top of the resist to reduce any effects from deposited charges during exposure.
3. Exchanging the substrate to InP, which should exhibit increased scattering in the substrate due to its higher density³⁶.

The measured PPSFs, their corresponding CDFs, and the fits of the PLG model to these experiments are shown in Fig. 6 together with the fit of the PLG model to the experiment shown in Figs. 3-5. The fit parameters for each of our experiments are summarized in table 1.

In the experiment with a longer development time, more resist is dissolved, so each hole of a

given shot dose, q_{in} , is developed out to a larger radius, r_0 . However, this is offset by a reduction in the clearing dose, D_0 , such that the PPSF remains approximately the same, as shown in Fig. 6(a)-(b).

Adding the decharging layer results in a slight broadening of the short-range PPSF, as shown in Fig. 6(c)-(d). The difference between currents remains. On the one hand, this indicates that this difference does not originate from charging effects and, on the other hand, that the effect of the thin decharging layer is negligible for exposure of thin resists at high acceleration voltages.

The long-range part of the PPSF is significantly different for the InP substrate as shown in Fig. 6(e)-(f), whereas the short- to intermediate-range distributions remain largely invariant between substrates. The decrease in β highlights that, without the power-law cutoff term in the

Table 1 Measured clearing doses, D_0 , integrals of the process point spread function (PPSF), $\max(\Phi)$, and fit parameters of the power-law plus Gaussian (PLG) model, β , η , γ , σ , and ν .

	D_0 $\mu\text{C cm}^{-2}$	$\max(\Phi)$	β μm	η	γ nm	σ	ν^a nm
Si	225(5)	0.88	59(4)	0.67(5)	15(2)	2.69(7)	24.9
Si L ^b	175(5)	0.89	56(3)	0.75(4)	17(2)	2.71(7)	27.3
Si Al	225(5)	0.84	60(5)	0.68(6)	19(3)	2.79(10)	28.9
InP	165(5)	0.93	23(1)	1.16(13)	12(2)	2.52(9)	22.2

^a ν values required for normalization with γ and σ best estimates.

^b Longer development time of 180 s instead of 60 s.

PLG model, the power-law term would dominate beyond β and result in a poor fit. Additionally, η increases significantly, which is evident from the CDF, and also leads to a decrease in D_0 . Essentially, the long-range scattering is stronger but shorter due to the increased electron scattering on the heavier elements in the InP substrate.

The effect of acceleration voltage on the process point-spread function

Finally, we explore the applicability of the PLG model for various acceleration voltages, V . We simulate the PSFs for 180 nm CSAR on silicon with $V=[5-150]$ kV and convolve them with a Gaussian with a full width at half maximum of 4 nm in order to estimate the PPSFs. The result is shown in Fig. 7(a) with the corresponding CDFs shown in Fig. 7(b). We observe that the short-range contribution is much less dependent on V than the long-range part. A fit of the PLG model for 150 kV is included as an example, and we refer to the Supporting Information for fits at other voltages. The fits capture the PPSFs accurately across all voltages. From the fits, we extract the parameters β , η , γ , σ , and ν of the PLG model as a function of V as shown in Fig. 7(c)-(g).

We note two distinct regimes, wherein the parameters η , γ , σ , and ν remain approximately constant for $V > 50$ kV but vary significantly for $V < 50$ kV. Conversely, β follows an approximately quadratic dependence across all acceleration voltages. At the lower voltages, β reduces from a few microns to a few hundred nanometers, such that the PPSFs likely vary significantly within the depth of the resist. Thus, we attribute the behavior at $V < 50$ kV to the fact that we average out the depth dependence of the PSFs in the output of our simulations. In contrast, when $V > 50$ kV the scattering length is high

compared to the resist thickness and the only variation with V is the increase in β , which simply shows that the same fraction of long-range dose is distributed across a larger area. The consequence of this is that PEC can be simpler for large V because the long-range scattering is approximately constant for patterns much smaller than β . However, the larger range also implies that PEC must correct for proximity doses over a much larger area. The remaining PLG model parameters stay constant at high V and highlight that the short- to intermediate-range proximity effects remain relevant for nanostructure fabrication.

Lastly, it should be noted that increasing V also reduces the total energy deposited by scattering, $E_{\text{tot}}(V) = 2\pi \int E(r, V) r dr$, which is the normalization constant of the PSF simulations, and inversely related to the clearing dose as

$$\frac{D_0(V)}{D_0(V_0)} = \frac{E_{\text{tot}}(V_0)}{E_{\text{tot}}(V)}, \quad (11)$$

with V_0 some fixed voltage. Hence, simulations of the electron scattering give estimates of $D_0(V)$, as shown in Fig. 7(h) with $V_0 = 150$ kV. The nearly linear dependence of $D_0(V)$ means that high acceleration voltages enable finer dose control at the cost of speed, which can be necessary in order to achieve increasingly smaller feature sizes.

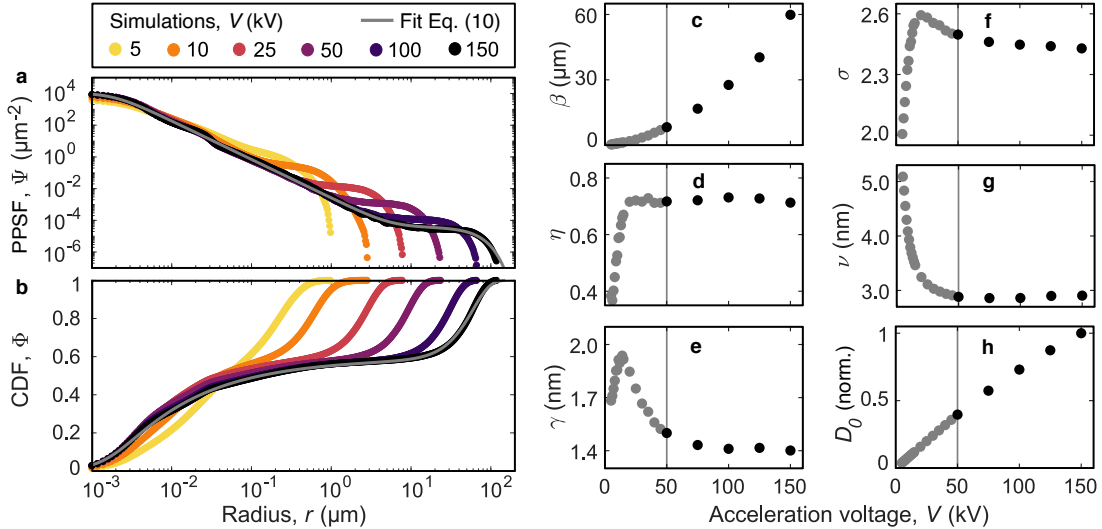


Figure 7 The dependence of the process point-spread function (PPSF) on acceleration voltage, V , in the range $V = 5$ – 150 kV for 180 nm CSAR on silicon. (a) Estimate of the PPSF for different voltages (colors). These are calculated by convolving the point-spread functions obtained from Monte Carlo simulations with a Gaussian of full width at half maximum 4 nm approximating the finite beam waist. The fit to the power-law plus Gaussian (PLG) model for $V = 150$ kV is also shown (grey line). (b) The cumulative density functions (CDFs) corresponding to the PPSFs. (c)–(g) The fitting parameters of the PLG model as a function of acceleration voltage. (h) The clearing dose calculated from the normalization of each simulation, normalized to $D_0(V_0)$ where $V_0 = 150$ kV, *cf.* Eq. 11. We observe that β and D_0 increase with V , while the remaining parameters, η , γ , σ , and ν remain approximately constant for $V > 50$ V (black dots) and vary significantly for $V < 50$ V (gray dots), which we attribute to three-dimensional effects as discussed in the main text.

Conclusions

We have measured the PPSF that characterizes the proximity effect in EBL. The PPSF, obtained from exposures of single shots and normalized by the pattern-independent clearing dose, shows excellent agreement with Monte Carlo simulations of the PSF, although we observe deviations in the regions limited by metrology or the number of data points. The CDF shows that a fraction of the deposited dose is unaccounted for in our measurements, stemming from either process or metrology effects.

The common 2G model deviates from experiments by more than four orders of magnitude, because it disregards the intermediate range of the PPSF. We therefore propose a PLG model, which shows excellent agreement with all the experiments and Monte Carlo simulations of PPSFs, independent of material stacks, development time, and acceleration voltages in the range 5 – 150 kV. This indicates that the PLG model can capture the key features of the PPSFs regardless of all microscopic details, while simultaneously offering the advantages of a simple model with interpretable parameters. This allows comparisons

between exposures, processes, and material platforms in order to obtain insights into the electron scattering and PEC.

We find that when the electron acceleration voltage is high in comparison to the resist thickness and electron scattering in the substrate, the long-range dose contribution of the PPSF is distinctly separated from its short- to intermediate-range contributions. The boundary is captured by the radius at which the two terms of the PLG model are equal, and can be used to make accurate simplifications for PEC. For a stack consisting of 180 nm resist on silicon, this thin-resist assumption is excellent for $V > 50$ V. In this regime, the short- to intermediate-range PPSF is well-described by a power law and largely unaffected by voltage, material stack, and development time. However, η remains constant for a given substrate while β increases with an approximately square dependence, implying that the relative long-range dose contribution remains the same, only distributed across longer distances. This potentially simplifies PEC because the long-range dose is approximately constant for distances $\ll \beta$, although larger areas need to be accounted for. The clearing

dose scales nearly linearly with voltage, enabling finer dose control at the cost of speed.

Remarkably, the short- to intermediate-range PPSF remains similar across all experiments and simulations. It reveals that, when the beam waist is narrow, the 2G model is inaccurate, and increasingly so at higher voltages. The complicated behavior of the PPSF at low voltages, which is likely due to three-dimensional effects, calls for further simulations and experiments. To determine the origin of the dose unaccounted for in the measured PPSFs, it would require additional careful measurements and characterization at higher resolutions. However, functions representing processes such as development, etching or deposition are not necessarily normalized or independent of pattern shape. Further measurements of such PPSFs could enable comprehensive inclusion of processing effects in PEC already during exposure.

Materials and methods

Samples consisting of 180 nm AllResist (Strausberg, Germany) AR-P 6200 (CSAR) on silicon and InP substrates are exposed using a 150 kV Elionix (Tokyo, Japan) ELS-F150 electron-beam writer. Each sample contains both point and area exposures: The pattern of point exposures is one array of shot charges q_{in} ranging from 1 fC to 5 μC at pitch $d = 140 \mu\text{m}$ and beam current $I = 10 \text{ nA}$, and an additional array with q_{in} from 1 fC to 10 pC with $d = 5 \mu\text{m}$ and $I = 0.1 \text{ nA}$. The pattern of area exposures is an array of squares of side lengths $b = 250 \mu\text{m}$, receiving a uniform exposure dose D_{in} in the range $180 \mu\text{C} \cdot \text{cm}^{-2}$ to $235 \mu\text{C} \cdot \text{cm}^{-2}$.

The samples are developed in single-puddle Zeon Corporation (Tokyo, Japan) ZED-N50 developer for 60 s before the developed radii, r_0 , are measured using scanning electron microscopy (SEM) and optical microscopy (OM). One sample with silicon substrate is instead developed for 180 s. Another sample with silicon substrate has a 20 nm aluminium decharging layer deposited on top of the resist before exposure. The layer is removed again after exposure, but prior to development of the resist, by development in single-puddle MicroChemicals GmbH (Ulm, Germany) AZ 726 MIF for 60 s.

Data availability

Data from the article is freely available at Zenodo, <https://zenodo.org/records/15691545>.

Acknowledgements

We gratefully acknowledge financial support from the Villum Foundation Young Investigator Program (Grant No. 13170), Innovation Fund Denmark (Grants No. 0175-00022 – NEXUS and No. 4356-00007B – EQUAL), the European Research Council (Grant No. 101045396 – SPOTLIGHT), the Horizon Europe Research and Innovation Programme (Grant No. 101098961 – NEUROPIC), and the Danish National Research Foundation (Grant No. DNRF147 – NanoPhoton).

Conflict of interests

S.S. declares his partial ownership of Beamfox Technologies ApS. N.B.H., K.S.K., M.A., T.S., and C.A.R. declare no conflict of interests.

Author contributions

Nikolaj Balslev Hougs: Writing—original draft, Writing—review and editing, Visualization, Methodology, Formal analysis, Data curation, Conceptualization. Kristian Sofus Knudsen: Writing—original draft, Writing—review and editing, Visualization, Methodology, Formal analysis, Data curation, Conceptualization. Marcus Albrechtsen: Writing—original draft, Writing—review and editing, Methodology, Data curation, Conceptualization, Supervision. Taichi Suhara: Methodology, Data curation, Conceptualization. Christian Anker Rosiek: Writing—review and editing, Conceptualization. Søren Stobbe: Writing—review and editing, Methodology, Conceptualization, Project administration, Funding Acquisition, Supervision.

Supporting Information

Details of the Monte Carlo simulations for obtaining point-spread functions, the image-analysis procedure used to extract the radii of developed holes, data sets and data analyses, details on the fitting procedure, and model fits for various acceleration voltages (PDF).

References

- [1] Smith, B., Rice, B., Groves, T. & Resnick, D. *Nanolithography* (Woodhead Publishing, 2014).
- [2] Bojko, R. J. *et al.* Electron beam lithography writing strategies for low loss, high confinement silicon optical waveguides. *J. Vac. Sci. Technol. B* **29**, 06F309 (2011).
- [3] Biswas, A. *et al.* Advances in top-down and bottom-up surface nanofabrication: Techniques, applications & future prospects. *Adv. Colloid Interface Sci.* **170**, 2–27 (2012).
- [4] Chou, S. Y., Krauss, P. R. & Renstrom, P. J. Nanoimprint lithography. *J. Vac. Sci. Technol. B* **14**, 4129 (1996).
- [5] Asano, M. *et al.* Metrology and inspection required for next generation lithography. *Jpn. J. Appl. Phys.* **56**, 06GA01 (2017).
- [6] Ikeno, R., Maruyama, S., Mita, Y., Ikeda, M. & Asada, K. Electron-beam lithography with character projection technique for high-throughput exposure with line-edge quality control. *J. Micro/Nanolithogr., MEMS, MOEMS* **15**, 031606 (2016).
- [7] Servin, I. *et al.* Progress and process improvements for multiple electron-beam direct write. *Jpn. J. Appl. Phys.* **56**, 06GC03 (2017).
- [8] Greve, M. M. & Holst, B. Optimization of an electron beam lithography instrument for fast, large area writing at 10 kV acceleration voltage. *J. Vac. Sci. Technol. B* **31**, 043202 (2013).
- [9] Mankiewich, P. M., Jackel, L. D. & Howard, R. E. Measurements of electron range and scattering in high voltage e-beam lithography. *J. Vac. Sci. Technol. B* **3**, 174 (1985).
- [10] Jones, G. A. C., Blythe, S. & H., A. Very high voltage (500 kV) electron beam lithography for thick resists and high resolution. *J. Vac. Sci. Technol. B* **5**, 120 (1987).
- [11] Tennant, D. M. Progress and issues in e-beam and other top down nanolithography. *J. Vac. Sci. Technol. A* **31**, 050813 (2013).
- [12] Gangnaik, A. S., Georgiev, Y. M. & Holmes, J. D. New generation electron beam resists: A review. *Chem. Mater.* **29**, 1898–1917 (2017).
- [13] Albrechtsen, M. *et al.* Nanometer-scale photon confinement in topology-optimized dielectric cavities. *Nat. Commun.* **13**, 6281 (2022).
- [14] Chang, T. H. P. Proximity effect in electron-beam lithography. *J. Vac. Sci. Technol.* **12**, 1271–1275 (1975).
- [15] Rishton, S. A. & Kern, D. P. Point exposure distribution measurements for proximity correction in electron beam lithography on a sub-100 nm scale. *J. Vac. Sci. Technol. B* **5**, 135 (1987).
- [16] Duan, H. *et al.* Sub-10-nm Half-Pitch Electron-Beam Lithography by Using Poly(Methyl Methacrylate) As a Negative Resist. *J. Vac. Sci. Technol. B* **28**, C6C58–C6C62 (2010).
- [17] Manfrinato, V. R. *Electron-Beam Lithography Towards the Atomic Scale and Applications to Nano-Optics*. Ph.D. thesis, Massachusetts Institute of Technology (2015).
- [18] Parikh, M. Self-consistent proximity effect correction technique for resist exposure (SPECTRE). *J. Vac. Sci. Technol.* **15**, 931–933 (1978).
- [19] Parikh, M. Corrections to proximity effects in electron beam lithography. I. Theory. *J. Appl. Phys.* **50**, 4371–4377 (1979).
- [20] P. Kern, D. Bakish, R. (ed.) *A novel approach to proximity effect correction*. (ed. Bakish, R.) *Electron and Ion Beam Science and Technology, Ninth International Conference*, Vol. 80, 326–339 (1980).
- [21] Owen, G. & Rissman, P. Proximity effect correction for electron beam lithography by equalization of background dose. *J. Appl.*

- Phys.* **54**, 3573–3581 (1983).
- [22] Pavkovich, J. M. Proximity effect correction calculations by the integral equation approximate solution method. *J. Vac. Sci. Technol. B* **4**, 159 (1986).
- [23] Abe, T. & Takigawa, T. Proximity effect correction for high-voltage electron beam lithography. *J. Appl. Phys.* **65**, 4428–4434 (1989).
- [24] Owen, G. Methods for proximity effect correction in electron lithography. *J. Vac. Sci. Technol. B* **8**, 1889 (1990).
- [25] Murai, F., Yoda, H., Okazaki, S., Saitou, N. & Sakitani, Y. Fast proximity effect correction method using a pattern area density map. *J. Vac. Sci. Technol. B* **10**, 3072 (1992).
- [26] Eisenmann, H., Waas, T. & Hartmann, H. PROXECCO—Proximity effect correction by convolution. *J. Vac. Sci. Technol. B* **11**, 2741 (1993).
- [27] Mack, C. A. Kawahira, H. (ed.) *Electron-Beam Lithography Simulation for Mask Making: VI. Comparison of 10- and 50-kV GHOST Proximity Effect Correction*. (ed. Kawahira, H.) *Photomask and Next-Generation Lithography Mask Technology VIII*, Vol. 4409, 194 – 203 (SPIE, 2001).
- [28] Donnelly, V. M. & Kornblit, A. Plasma etching: Yesterday, today, and tomorrow. *J. Vac. Sci. Technol. A* **31**, 050825 (2013).
- [29] Hess, D. W. & Jensen, K. F. Chemical Vapor Deposition. *Adv. Chem.* **221**, 199–263 (1989).
- [30] Ahmad, R. *et al.* Deposition of nanomaterials: A crucial step in biosensor fabrication. *Mater. Today Commun.* **17**, 289–321 (2018).
- [31] Kanaya, K. & Okayama, S. Penetration and energy-loss theory of electrons in solid targets. *J. Phys. D: Appl. Phys.* **5**, 43–58 (1972).
- [32] Messina, G., Paoletti, A., Santangelo, S. & Tucciarone, A. Electron scattering in microstructure processes. *Riv. Nuovo Cim.* **15**, 1–57 (1992).
- [33] Manfrinato, V. R. *et al.* Determining the Resolution Limits of Electron-Beam Lithography: Direct Measurement of the Point-Spread Function. *Nano Lett.* **14**, 4406–4412 (2014).
- [34] Randall, J. N., Owen, J. H. G., Lake, J. & Fuchs, E. Next generation of extreme-resolution electron beam lithography. *J. Vac. Sci. Technol. B* **37**, 061605 (2019).
- [35] Saitou, N. Monte Carlo Simulation for the Energy Dissipation Profiles of 5–20 keV Electrons in Layered Structures. *Jpn. J. Appl. Phys.* **12**, 941–942 (1973).
- [36] Hawryluk, R. J., Hawryluk, A. M. & Smith, H. I. Energy dissipation in a thin polymer film by electron beam scattering. *J. Appl. Phys.* **45**, 2551–2566 (1974).
- [37] Johnson, S. & MacDonald, N. C. A program for Monte Carlo simulation of electron energy loss in nanostructures. *J. Vac. Sci. Technol. B* **7**, 1513 (1989).
- [38] Agostinelli, S. *et al.* Geant4—a simulation toolkit. *Nuclear Instruments and Methods in Physics Research Section A: Accelerators, Spectrometers, Detectors and Associated Equipment* **506**, 250–303 (2003).
- [39] Clauset, A., Shalizi, C. R. & Newman, M. E. J. Power-law distributions in empirical data. *SIAM Rev.* **51**, 661–703 (2009).
- [40] Saitou, N., Munakata, C. & Honda, Y. Change of Apparent Sensitivity of an Electron Resist Due to Backing Materials. *Jpn. J. Appl. Phys.* **11**, 1061–1062 (1972).
- [41] Yu, H., Yu, J., Sun, F., Li, Z. & Chen, S. Systematic considerations for the patterning of photonic crystal devices by electron beam lithography. *Opt. Commun.* **271**, 241–247 (2007).

- [42] Florez, O. *et al.* Engineering nanoscale hyper-sonic phonon transport. *Nat. Nanotechnol.* **17**, 947–951 (2022).
- [43] Lee, S., Jacob, J. C., Chen, C., McMillan, J. A. & MacDonald, N. C. Proximity effect correction in electron-beam lithography: A hierarchical rule-based scheme—PYRAMID. *J. Vac. Sci. Technol. B* **9**, 3048 (1991).
- [44] Sewell, H. Control of pattern dimensions in electron lithography. *J. Vac. Sci. Technol.* **15**, 927–930 (1978).
- [45] Eunsung Seo, E. S. & Ohyun Kim, O. K. Dose and Shape Modification Proximity Effect Correction for Forward-Scattering Range Scale Features in Electron Beam Lithography. *Jpn. J. Appl. Phys.* **39**, 6827 (2000).
- [46] Liu, C.-H. *et al.* Alek C. Chen, A. Y., Burn Lin (ed.) *A novel curve-fitting procedure for determining proximity effect parameters in electron beam lithography.* (ed. Alek C. Chen, A. Y., Burn Lin) *Lithography Asia 2008*, Vol. 7140, 367 – 376 (2008).
- [47] Kotera, M. & Maekawa, T. Simulation of fogging electrons in electron beam lithography. *Jpn. J. Appl. Phys.* **48** (2009).
- [48] Bickford, J. R., Lopez, G., Belic, N. & Hofmann, U. Hydrogen silsesquioxane on SOI proximity and microloading effects correction from a single 1D characterization sample. *J. Vac. Sci. Technol. B* **32**, 06F511 (2014).
- [49] Schirmer, M. *et al.* Uwe F. W. Behringer, W. M. (ed.) *Chemical semi-amplified positive e-beam resist (csar 62) for highest resolution.* (ed. Uwe F. W. Behringer, W. M.) *29th European Mask and Lithography Conference*, 88860D (2013).

Measurements, simulations, and models of the point-spread function of electron-beam lithography

Nikolaj B. Hougs^{1*}, Kristian S. Knudsen¹, Marcus Albrechtsen¹, Taichi Suhara²,
Christian A. Rosiek¹, Søren Stobbe^{1,3,4}

¹DTU Electro, Department of Electrical and Photonics Engineering, Technical University of Denmark, Ørstedes Plads 343, Kgs. Lyngby, DK-2800, Denmark.

²ELIONIX INC., 3-7-6 Motoyokoyama-cho Hachioji, Tokyo, 192-0063 Japan.

³NanoPhoton — Center for Nanophotonics, Technical University of Denmark, Ørstedes Plads 343, Kgs. Lyngby, DK-2800, Denmark.

⁴Beamfox Technologies ApS, Njalsgade 76, 4., Copenhagen S, DK-2300, Denmark.

*Corresponding author(s). E-mail(s): nibaho@dtu.dk;

Obtaining the electron point-spread function from Monte Carlo simulations of electron scattering

For this work we have used a Geant4-based Monte Carlo simulation of electron scattering¹⁻³. In such a simulation, we consider a resist of depth z_0 on a substrate as in Fig. 1(a) of the main text. When simulating the electron scattering, it is typically the energy density deposited in the resist, $\tilde{E}(r, z)$, with $0 < z < z_0$, that is obtained. In general, the electron point-spread function (PSF) is then extracted as

$$\tilde{\Psi}(r, z) = \frac{\tilde{E}(r, z)}{2\pi \int \int \tilde{E}(r, z) r dr dz} = \frac{\tilde{E}(r, z)}{\tilde{E}_{\text{tot}}}. \quad (1)$$

In cases of thin resist, the PSF is considered invariant in the vertical direction and approximated as an area density

$$\Psi(r) \approx \int_0^{z_0} \tilde{\Psi}(r, z) dz \approx z_0 \tilde{\Psi}(r, z_{\text{res}}), \quad (2)$$

with z_{res} an arbitrary depth within the resist. This approximation is included in the output of our simulations, except those shown in Fig. 2(b) and (c) of the main text. The same approximation can be similarly applied to $\tilde{E}(r, z) \rightarrow E(r)$ in order to obtain Eq. (1) of the main text. Note that this changes the units from $[\tilde{\Psi}] = \text{m}^{-3}$ and $[\tilde{E}] = \text{eV} \cdot \text{m}^{-3}$ to $[\Psi] = \text{m}^{-2}$ and $[E] = \text{eV} \cdot \text{m}^{-2}$.

The beam distribution can be included at the simulation stage, but we recommend simulating the deposited energy and PSF from electron scattering of a δ -function beam, $\tilde{\Psi}_{\text{scat}}(r, z)$, after which an arbitrary beam distribution, $\Psi_{\text{beam}}(x, y)$, can be convoluted to find the process-specific PSF (PPSF)

$$\Psi(x, y) = z_0 \tilde{\Psi}_{\text{scat}}(r, z_{\text{res}}) * \Psi_{\text{beam}}(x, y). \quad (3)$$

Any further fabrication steps, such as development or etching, can then be accounted for by further convolutions with appropriate functions, in order to simulate an arbitrary PPSF.

Image analysis to extract the radii of developed holes

We estimate the radii of holes in the developed resist using an automatic image-analysis process, seeking consistent estimates of radii for the hundreds of images we analyze. The input data are scanning electron microscopy (SEM) or dark-field optical microscopy (OM) images, such as Fig. (4)(b)-(d) in the main text. The result is deterministic given the same input image and parameters for the analysis but may be affected by the imaging settings and the slope of the sidewalls. In dark-field OM, topographical variations such as edges or roughness appear bright. In SEM, features appear brighter when the electron beam penetrates material adjacent to an edge, in which case secondary electrons can escape and be detected⁴. Based on this, the inner transition from dark to bright is chosen as the estimate for the developed hole radius, although the true radius may be slightly offset or, in some cases, gradual. In any case, a rigorous definition of how to extract the hole radius is needed. The following is a summarized description of the automatic image-analysis process:

1. Denoising: Noise in the input image severely hinders the following steps if not removed. Sharp edge features can be preserved while removing high-frequency noise by denoising using anisotropic diffusion⁵, as shown in Fig. 1(a).
2. Pre-processing: A gradient filter (Sobel) applied to the denoised image results in a gradient image as shown in Fig. 1(b). A threshold is applied to binarize the gradient image, then all pixels not connected to the ring-shaped inner edge of the circular hole are removed, as shown in Fig. 1(c).
3. Circle-finding: A Circular Hough Transform, a slow but accurate shape-detection algorithm, is performed on the binary image for various test radii to estimate the circle center and radius.
4. Refined estimate: The pixel intensities on the gradient image are integrated radially from the estimated center of the circle, giving graphs as in Fig. 1(d) that are resilient against minor errors in the initial center estimates. The final radius is estimated as the peak corresponding to the inner edge of the hole.

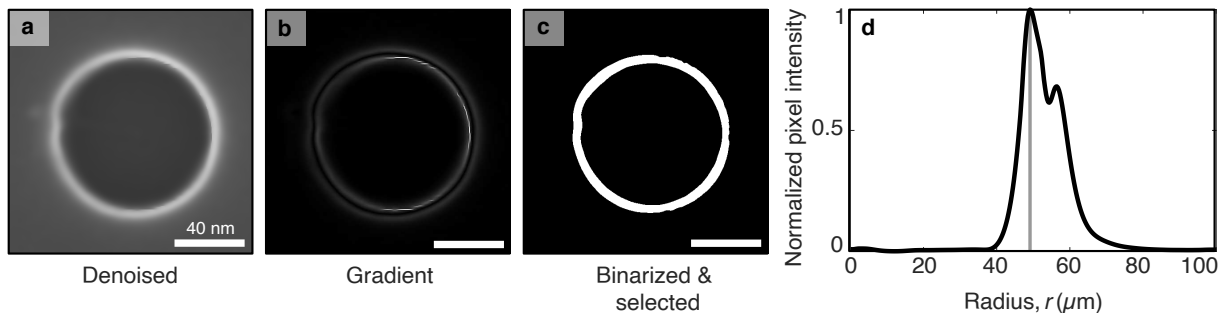


Figure 1 Image-analysis process to determine the radii of developed holes. (a) First, the input image is denoised by anisotropic diffusion (100 iterations, local contrast $K = 0.05$, and conduction coefficient weight $\lambda = 0.2$)⁵, (b) then a Sobel filter which produces a discrete approximation of the magnitude of the gradient is applied. (c) Thresholding of the gradient image and removing select pixel groups allows isolation of the circle of interest, whose center is found using a Circular Hough Transform. (d) Lastly, the pixel intensities of the gradient image, integrated wrt. radius and normalized, gives peaks corresponding to the inner and outer edge of the bright circle in the input image, where the inner peak is estimated as the resist-substrate interface.

Additional details on the data sets and analysis

We use a low current of $I = 0.1$ nA for the point exposures shown in Figs. (4)-(6) except for the largest doses where a higher current of $I = 10$ nA was chosen to reduce the write time. The two SEM data sets agree well except at very small radii, because the different exposure currents result in physically different hole sizes. Alternatively, fast and easy measurements devoid of charging artefacts can be obtained from OM, which agrees well with the SEM data for large radii but becomes too inaccurate for smaller radii. We therefore discard the data points for $I = 10$ nA below 50 nm and the OM data below 2 μ m when calculating the cumulative density functions (CDFs) and fitting models. In Fig. (4)(f), the OM data point at 7 μ m is inconsistent with the corresponding SEM data point at 25 μ m and is likewise discarded. The discrepancy stems from the different contrast mechanisms in the two imaging methods in the case of a hole with a particularly low and rough sidewall slope.

Power-law plus Gaussian model fits at different acceleration voltages

We first note that power laws are generally difficult to fit well⁶. Since the PPSF spans several orders of magnitude from nanometer to micrometer scale, one issue is that simple least-squares fitting is biased towards data points at lower radii, as these have higher values and are more dense, thus producing far larger errors. The issue stemming from the significant range of the vertical axis can be avoided by fitting the CDF, but this is troublesome without an analytical CDF, as is the case with the PLG model. Instead, we fit to the PPSF in log-log space to minimize the relative residuals

$$R = \sum_j \hat{r}_j^2 \Delta \hat{r}_j^2 [\hat{\Psi}_j(\hat{r}_j) - \hat{\Psi}_{\text{PLG}}(\hat{r}_j)]^2, \quad (4)$$

$$\Delta \hat{r}_j = (\hat{r}_{j+1} - \hat{r}_{j-1})/2, \quad (5)$$

where \hat{r} indicates $\log_{10}(r)$ and the weights $\Delta \hat{r}_j$ approximate areas of rings with radii \hat{r}_j and widths $\Delta \hat{r}_j$, as a log-scale approach to the weights used by Rishton and Kern⁷. However, the power-law term of the PLG model is only normalized by selecting a value for ν , so directly fitting the parameters can give incorrect ν and η . For this reason, we first obtain an initial fit that is close to, but not normalized. Then we scale ν to obtain a normalized but incomplete fit. Lastly, we fit to the CDF to obtain η , by keeping the remaining parameters from the incomplete fit constant.

Figure 2 shows examples of such PLG model fits to simulated PSFs and corresponding CDFs for acceleration voltages 5-150 kV. The fit parameters are included in Table 1, along with the normalization constant of the simulations. Notably, the two model terms are poorly distinguishable at 5-10 kV, making estimates for η in this range less interpretable as the ratio between a distinct long-range contribution and other dose contributions.

Table 1 Point-spread-function parameters obtained from simulations of electrons impinging on a stack comprising 180 nm CSAR on silicon at different acceleration voltages, V : Energy deposited per electron, E_{tot}/e^- , and fit parameters of the power-law plus Gaussian (PLG) model, β , η , γ , σ , and ν .

V kV	E_{tot}/e^- eV	β μ m	η	γ nm	σ	ν^a nm
5	1241	0.32(2)	0.38(4)	1.68(6)	2.01(2)	5.1
10	617	0.81(1.0)	0.53(6)	1.86(9)	2.37(4)	3.9
25	242	2.57(2)	0.72(4)	1.85(5)	2.58(2)	3.1
50	122	8.27(9)	0.72(5)	1.50(5)	2.50(2)	2.9
100	66	27.7(3)	0.73(4)	1.41(4)	2.45(1.3)	2.9
150	48	60(1.4)	0.71(3)	1.40(4)	2.43(1.1)	2.9

^a ν values required for normalization with the shown γ and σ estimates.

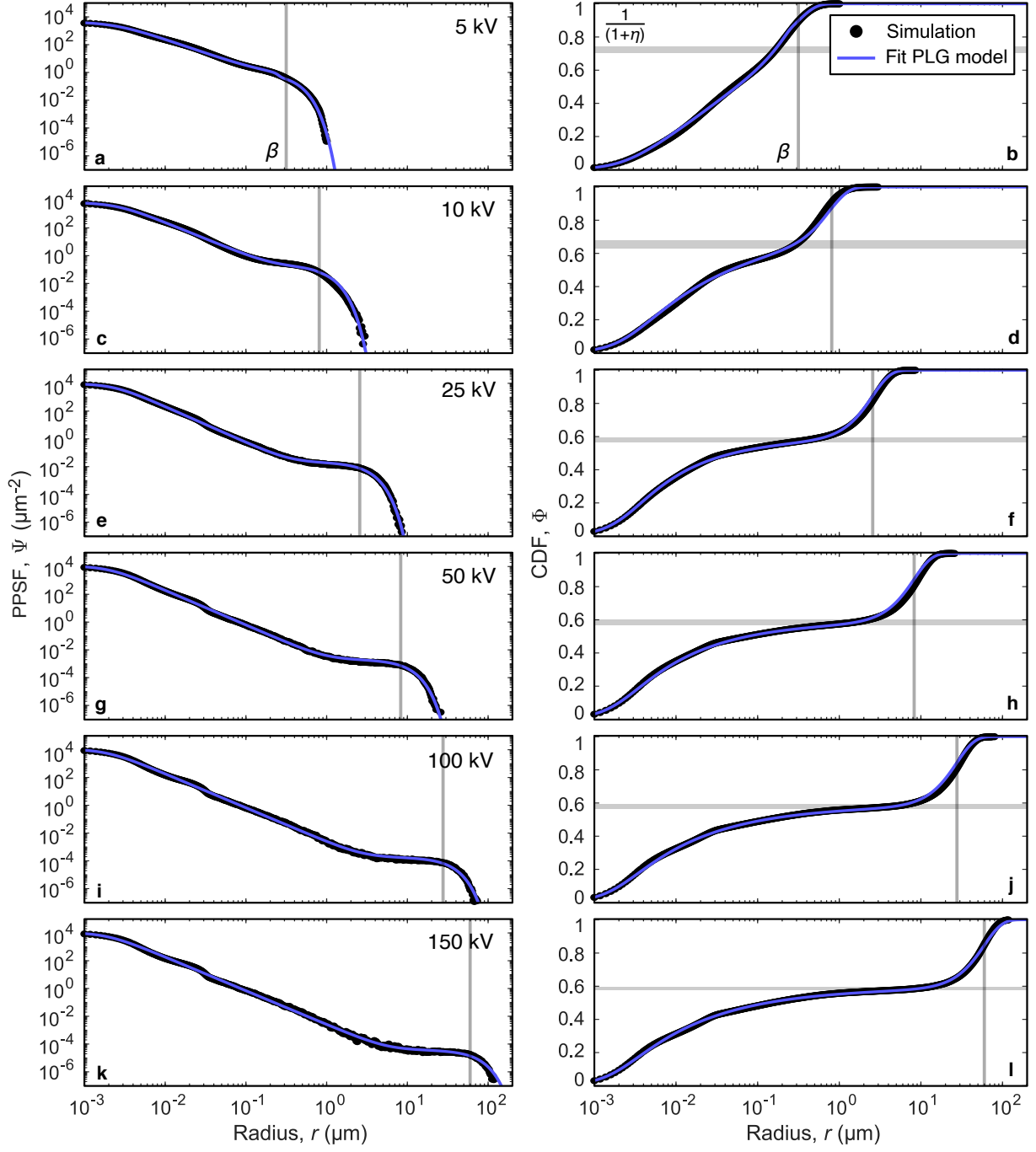


Figure 2 Fits to Monte-Carlo simulations of the PSF with the power-law plus Gaussian (PLG) model. (left) Simulated electron point-spread functions in 180 nm CSAR on silicon with increasing electron acceleration voltage, V . (right) Corresponding cumulative density functions. The PLG model provides excellent fits in all cases. The gray lines indicate (vertical) β and (horizontal) the fraction of dose deposited at short to intermediate range, $1/(1+\eta)$. At low V , there is a less distinct separation between power-law and Gaussian behavior. As V increases, the model parameter β grows and η stabilizes.

References

- [1] Agostinelli, S. *et al.* Geant4—a simulation toolkit. *Nuclear Instruments and Methods in Physics Research Section A: Accelerators, Spectrometers, Detectors and Associated Equipment* **506**, 250–303 (2003).
- [2] Allison, J. *et al.* Geant4 developments and applications. *IEEE Transactions on Nuclear Science* **53**, 270–278 (2006).
- [3] Allison, J. *et al.* Recent developments in Geant4. *Nuclear Instruments and Methods in Physics Research Section A: Accelerators, Spectrometers, Detectors and Associated Equipment* **835**, 186–225 (2016).
- [4] Frase, C. G., Gnieser, D. & Bosse, H. Model-based sem for dimensional metrology tasks in semiconductor and mask industry. *Journal of Physics D: Applied Physics* **42**, 183001 (2009).
- [5] Perona, P. & Malik, J. Scale-space and edge detection using anisotropic diffusion. *IEEE Trans. Pattern Anal. Mach. Intell.* **12**, 629–639 (1990).
- [6] Clauset, A., Shalizi, C. R. & Newman, M. E. J. Power-law distributions in empirical data. *SIAM Rev.* **51**, 661–703 (2009).
- [7] Rishton, S. A. & Kern, D. P. Point exposure distribution measurements for proximity correction in electron beam lithography on a sub-100 nm scale. *J. Vac. Sci. Technol. B* **5**, 135 (1987).